



Properties of AgBiI₄ using high through-put DFT and machine learning methods

Cite as: J. Appl. Phys. **131**, 245701 (2022); <https://doi.org/10.1063/5.0088980>

Submitted: 21 February 2022 • Accepted: 31 May 2022 • Published Online: 22 June 2022

Victor T. Barone,  Blair R. Tuttle and  Sanjay V. Khare



View Online



Export Citation



CrossMark

Journal of Applied Physics **Special Topics** Open for Submissions [Learn More](#)

Properties of AgBiI_4 using high through-put DFT and machine learning methods

Cite as: J. Appl. Phys. 131, 245701 (2022); doi: 10.1063/5.0088980

Submitted: 21 February 2022 · Accepted: 31 May 2022 ·

Published Online: 22 June 2022



View Online



Export Citation



CrossMark

Victor T. Barone,¹ Blair R. Tuttle,^{2,a)}  and Sanjay V. Khare¹ 

AFFILIATIONS

¹Department of Physics, University of Toledo, Toledo, Ohio 43606, USA

²Department of Physics, Penn State Behrend, Erie, Pennsylvania 16563, USA

^{a)}Author to whom correspondence should be addressed: brt10@psu.edu

ABSTRACT

Silver iodo-bismuthates show promise for optoelectronic and other applications. Within this family of materials, AgBiI_4 is a prominent model compound. The complexity of AgBiI_4 has prevented a conclusive determination of specific atomic arrangements of metal atoms in the bulk material. Here, we employ high through-put density functional and novel machine learning methods to determine physically relevant unit cell configurations. We also calculate the fundamental properties of the bulk material using newly discovered configurations. Our results for the lattice constant (12.7 Å) and bandgap (1.8 eV) agree with the previous theory and experiment. We report new predictions for the bulk modulus (7.5 GPa) and the temperature-dependent conductivity mass for electrons (m_0 at $T = 300$ K) and holes ($7m_0$ at $T = 300$ K); these masses will be useful in AgBiI_4 -based device simulations.

Published under an exclusive license by AIP Publishing. <https://doi.org/10.1063/5.0088980>

I. INTRODUCTION

Metal halide semiconductors are a promising new class of materials under development for various applications including flexible electronics, optoelectronics, and radiation detectors.^{1–5} Specifically, silver iodo-bismuthates—i.e., compounds with a generic formula $\text{Ag}_x\text{Bi}_y\text{I}_{x+3y}$ —have captured significant research interest as a safer alternative to mainstream lead-halide perovskite semiconductors. Importantly, these compounds can be grown through simple, low-cost, solution-based methods in thin films over flexible substrates.^{4,6–8} Because they are good photon absorbers, these materials hold promise for a variety of optoelectronic devices, including photovoltaics and photodetectors.^{6–9}

The structure^{6,10} and phase diagram¹¹ of Ag–Bi–I crystals have only recently been examined in detail. Given that the unit cells are large and Ag–Bi atoms are site disordered, many calculations are needed to fully enumerate the possible unit cells of these crystals.⁸ Here, we focus on AgBiI_4 , a prominent embodiment of the silver iodo-bismuthate family, which has been found to display a cubic crystal structure in many of its occurrences.^{6,10,12} For AgBiI_4 , the singly valent metal cation is Ag, the triply valent cation is Bi, and the singly valent anion is I. Other compounds, such as AgBi_2I_7 , appear to be silver-deficient versions of cubic AgBiI_4 .¹⁰

Despite the importance of AgBiI_4 , the atomic positions for the Ag and Bi atoms in the crystal have not been clearly established, mainly because of the complexity of the unit cell. The AgBiI_4 crystals studied include cubic unit cells with two fixed sublattices; one sublattice includes iodine (I) atoms and the other includes Ag and Bi atoms. Because of the site-disorder in the position of Ag and Bi atoms, there are thousands of possible unit cell configurations that can make up the bulk crystal. For AgBiI_4 , previous calculations have employed a few sample structures and found structural properties and electronic bandgaps in agreement with experiments.^{10,12} Despite these early successes, to confidently predict AgBiI_4 properties, e.g., for defects observed therein,¹³ requires a clear understanding of the atomic structures present in device quality materials.

To identify the atomic positions in AgBiI_4 crystals and to clarify the crystal properties, we sorted all possible unit cell configurations from low to high energy. During growth conditions, we find that approximately 60 unit cells will be most present in bulk AgBiI_4 . Using hybrid density functional methods, including spin-orbit coupling, we calculate the bandgap to be 1.8 eV, in agreement with the experiments. We report the average electronic density of states (DOS) for AgBiI_4 and determine the temperature-dependent conductivity masses. For both electrons and holes, mass increases with temperature.

II. CELLS AND METHODS

A. Unit cells

Experimentally, AgBiI₄ has been reported to have a unit cell with a space group of Fd3m with cubic symmetry, a space group of R3m with trigonal symmetry, or a space group of C2/m with monoclinic symmetry.^{6,10} Here, we only consider the Fd3m-based unit cells with a cubic-closed packed sub-lattice of 32 iodine atoms and a cation sublattice with all tetrahedral sites vacant. The cation sub-lattice has 16 sites and each site can have either a bismuth (Bi) or a silver (Ag) atom. To determine the number of combinations that are possible, we use the binomial equation. In general, for n sites with k sites occupied by Bi atoms and $n - k$ sites occupied by Ag atoms, the number of combinations (C_k^n) can be written as $C_k^n = \frac{n!}{k!(n-k)!}$. In this case, with $n = 16$ and $k = 8$, there are 12 870 possible unit cell configurations, although many are equivalent by symmetry operations. For finding symmetry groups, we used SpGLib,¹⁴ which found that 72% of the cells had no symmetry (P1). If the distribution of actual cells present in device quality films is controlled by thermodynamics, then the low energy cells will be most prevalent. Figure 1(a) shows a ball-and-stick representation of the lowest energy unit cell for AgBiI₄, based on the results of our calculations discussed below. Figure 1(b) shows atomic positions of the same cell cut in slices along the c axis, which is the vertical axis in Fig. 1(a). In both images, the small black balls are iodine, the blue balls are bismuth, and the gray balls are silver atoms.

B. High through-put method

This article's overall workflow is summarized in Fig. 2. We use the Vienna *Ab Initio* Simulation Package (VASP)^{15–17} (version 5.4.1) for density functional calculations.^{18,19} We treat exchange-correlation effects with the semi-local Perdew–Burke–Ernzerhof (PBE) functional.²⁰ Standard PAW potentials are used to represent the core-electrons;^{21,22} for silver 4d¹⁰ 5s¹, bismuth 6s² 6p³ and iodine 5s² 5p⁵ were treated as valence electrons. For plane-wave basis function expansion, the cutoff energy used is 250 eV. Tests using a higher cutoff indicate that the physical properties of interest are well converged; e.g., lattice constants are converged to less than 1%.

Since there are over 12 000 unit cells to consider, a direct accurate DFT calculation of the relaxed energy of all the cells would be prohibitive. Therefore, we determine low-energy unit cell structures following a multi-step process where the accuracy of the method is increased as the number of cells considered is decreased. We have written our own set of programs for managing large numbers of VASP simulations called VBHTC.²³ The code creates VASP input files, automatically submits jobs to a computer with resources shared among multiple users, checks for job completion, and resubmits jobs automatically. The method employed here is similar to high through-put methods used previously.^{24,25}

For initial screening, we use an efficient PBE-based relaxation method. Specifically, only the Gamma point is used for Brillouin zone integrations and the unit cell lattice constants are fixed at the experimental value. Atomic positions are relaxed until forces reach a tolerance of 0.05 eV/Å. From these initial calculations, low-energy structures were identified for further consideration.

For final relaxations, we employ a more accurate PBE-based method. A single special k-point at $\frac{1}{4}$ (111) is used for improved convergence (this special k-point represents the average band energy better than the Γ point, which is usually located at a band energy extrema). With these calculation parameters, we also compute the lattice parameters and bulk modulus of each cell. For 60 lowest energy cells, further relaxations were performed including a $3 \times 3 \times 3$ k-point grid and a force tolerance of 0.01 eV/Å for atomic relaxations.

C. Analysis methods

Physical properties such as lattice parameters, simulated x-ray diffraction (XRD) patterns, density of states (DOS), and bulk moduli are determined as the average of the 60 lowest energy unit cells. The density of electronic states for select cells was evaluated on a $4 \times 4 \times 4$ k-point mesh at the PBE level. Note that in the VASP code, the Fermi level is placed at the top of the valence band for each cell, so the DOS averaging of several cells is properly aligned. A correction to the PBE bandgap was determined with a second set of calculations using a $2 \times 2 \times 2$ k-point mesh and the inclusion of hybrid exchange²⁶ and spin-orbit coupling.

The effective masses are calculated at the PBE level as a thermal average over all bands and over the entire Brillouin zone, as described by Hautier *et al.*²⁷ This method considers bands that are close to one another and non-parabolic bands. This is, especially, important for valence bands in AgBiI₄. The Brillouin zone integration was performed on a $91 \times 91 \times 91$ grid with k values interpolated as weighted averages between the less densely packed PBE calculated k -points.

D. Machine learning method

The computational cost of finding the energy of thousands of unit cells is prohibitive. Also, for other Ag–Bi–I systems, the number of unit cells to be considered is orders of magnitude larger. Therefore, we developed a machine learning method to reduce the computational load for finding low-energy cells. The method employs a Random Forest (RF) model from Python's scikit-learn package.²⁸ The features of the RF model include Ag or Bi at each of the 16 cation sites along with the number of neighbors for each metal pair. Other features such as the center of mass and the space group identifiers were tested but provided little additional benefit. The low-energy cells were discovered using the VBHTC²³ code for coupling the RF and VASP calculations in a high through-put fashion.

Three RF implementations were tested to search for the lowest energy unit cells. VASP Γ -point results were used for training all RF models. In version 1, the site occupancies were included in the RF feature set but without any description of the neighbor pair counts. In version 2, the neighbor pair counts were added to the feature set. In version 3, the feature set is the same as in version 2, but the RF model is forced to train on low-energy unit cells. Specifically, version 3 uses the following routine: (1) Initialize the RF model with a random set of 100 unit cell results from the total. (2) Use the RF model to predict energies of the remaining unit cells. (3) Keep (around) 20% of the unit cells with predicted lowest energy structures. (4) Choose 100 cells from the kept set to add

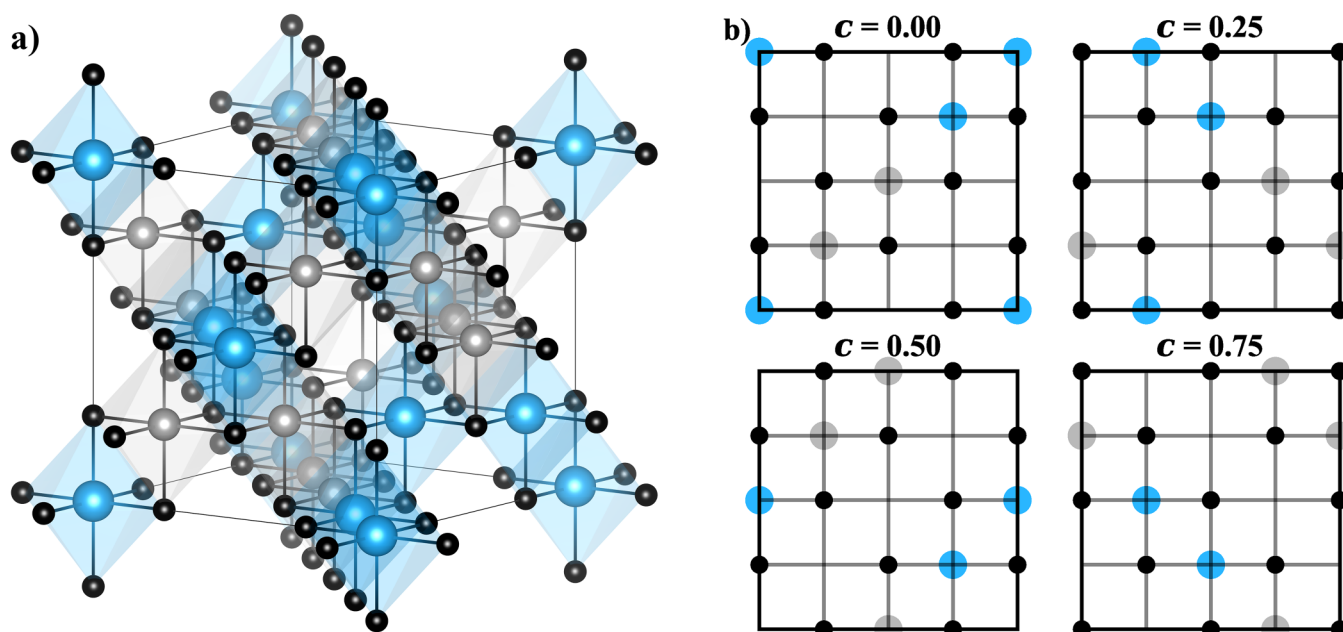


FIG. 1. (a) A ball-and-stick representation of the lowest energy unit cell discovered in this investigation. The shaded regions show the silver- and bismuth-centered octahedra. (b) The same unit cell represented as layers on the c axis to show the topology more clearly. In both images, the small black balls are iodine, the blue balls are bismuth, and the gray balls are silver atoms. Note that $c = 0.00 = c = 1.00$.

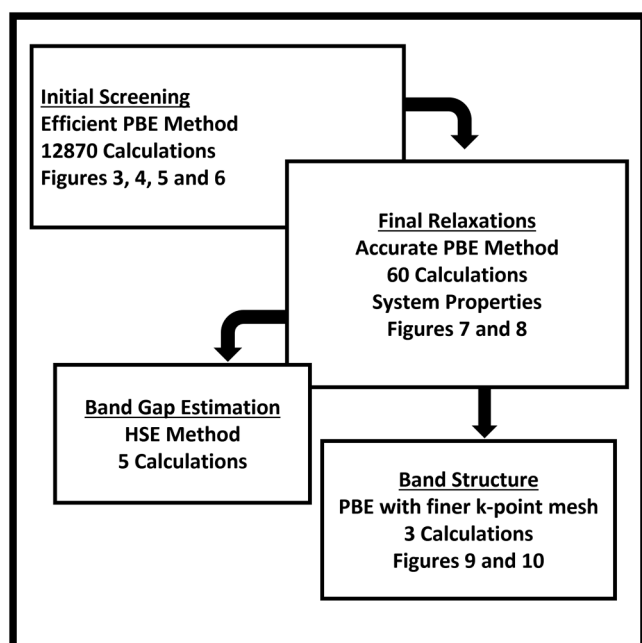


FIG. 2. Workflow of this study as described in Sec. II.

(not replace) to the RF model's training data. (5) With the trained RF model, re-estimate the energies of all unit cells. (6) repeat steps (3)–(5) until 20% of the kept set includes less than 100 unit cells.

Reducing the search space as described in version 3 is beneficial in that it significantly reduces the number of DFT calculations needed to find minimum energy structures. Technically, we aim to overfit the RF model to very accurately describe low-energy cells. In other applications, such as the prediction of phase diagrams, the accuracy of the RF model over a larger set of cells may be important. For our purposes, the higher energy cells need to be described with an accuracy just good enough to differentiate them from the lower energy cells.

III. PRELIMINARY RESULTS

Our initial energy calculations for all possible AgBiI_4 unit cells result in detailed information about the unit cell energetics and its relation to bonding topology. In addition, we present the energetics predicted by three random forest models and compare them to the DFT results.

A. Energetics

The initial screening of all 12 870 AgBiI_4 unit cell structures allows us to organize each unit cell according to its energy. In Fig. 3, an energy histogram is reported, which shows that the unit cell energies span about 3 eV from the lowest to highest energy cells. The peak of the histogram occurs at around 1 eV above the minimum energy. Over 12 800 unit cells are more than 0.25 eV

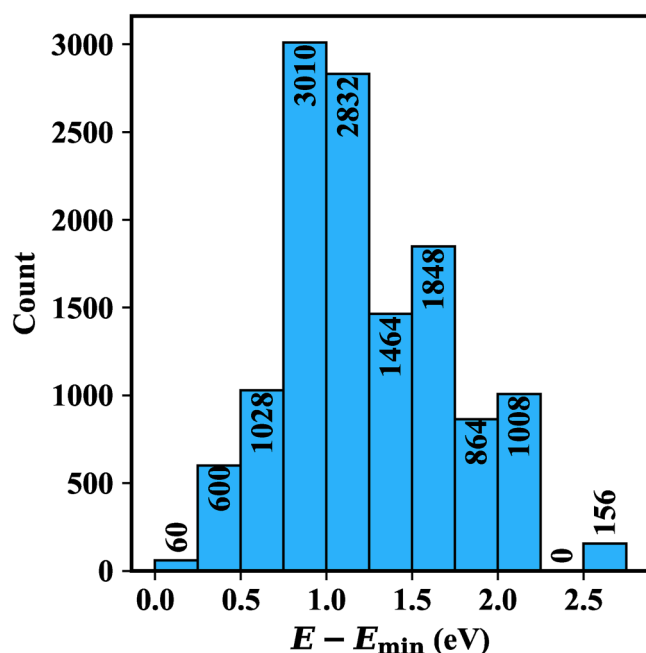


FIG. 3. Energy histogram for all possible AgBiI_4 unit cells. The energy E is relative to the minimum cell energy, E_{\min} . The number of cells in each bin is shown at the top of the bin.

above the energy of the minimum energy cells and are expected to be less important in bulk samples of AgBiI_4 . For the prediction of physical properties in Sec. IV, we only kept the 60 unit cells found in the lowest energy bin in Fig. 3.

The 60 unit cells can be split into two energy groups. The two groups are 0.11 eV apart from one another. Within those groups, the energy difference between cells is 1 meV or less. Further analysis of the lowest-energy group (which includes 12 unit cells) reveals that, from their initial coordinates, they are equivalent to one another through translational and rotational symmetry.¹⁴ The higher energy group's structures are significantly more complex than that of the lower energy groups, as discussed below.

We performed an analysis of metal pairs in order to better understand the role of these atoms on the energetics of AgBiI_4 . For Ag and Bi atoms, we define nearby metal neighbors to be within 4.5 Å of one another. Interestingly, the number of initial Ag–Ag pairs (before any relaxations) is a good indicator of final relative energies, as seen in Fig. 4. While all 12 870 results are included in the figure, many data points overlap. The number of Ag–Bi and Bi–Bi pairs is also a good indicator, as they are directly related to the number of Ag–Ag pairs. The same relation gives an identical slope of 0.32 eV for Bi–Bi pairs. Also, there is a slope of -0.16 eV for Ag–Bi pairs.

The number of Ag–Ag and Bi–Bi interactions is strongly correlated to the energy of the unit cell structure. The correlation illustrated in Fig. 4 is consistent with the chemical principle that ionic bonds are favored over metallic ones in materials containing atoms

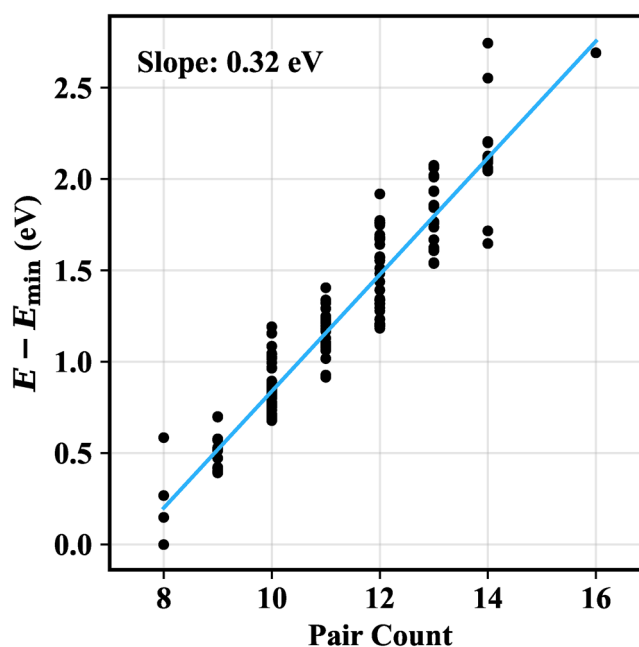


FIG. 4. Relation between post-relaxation energy E (scaled by the minimum E_{\min}) and pre-relaxation Ag–Ag pair counts. Each additional Ag–Ag pair increases the final energy by 0.32 eV on average.

with varying electronegativities. As discussed in Secs. II D and III B, the pair count info is essential for creating an efficient RF model. Although ionic atom relaxations lowered system energies considerably, the lowest energy cells were clearly those that started in a favorable state. In the lowest energy cells, each cation has exactly two identical-element pairs, which minimizes the total pair count for the entire cell to 8. Variance in the energy–pair count relationship shown in Fig. 4 is due to ionic relaxations.

The ionic relaxations in a cell are correlated to its energetics, with low-energy cells having low relaxation energies (the differences in energies between the initial and final states of the cells). Ag showed the most relaxation due in part to it being the lightest/smallest of the three elements. Over all 12 870 cells, the average (maximum) relaxation values from ideal positions for Ag, Bi, and I ions were 0.35 (0.98), 0.14 (0.29), and 0.14 (0.44) Å, respectively; for the 60 unit cells with the lowest energy, the same atomic relaxation values are 0.12 (0.21), 0.07 (0.09), and 0.10 (0.17) Å, respectively.

The topological properties of the neighbor chains are interesting. Figure 5 shows the Ag–Ag (gray) and Bi–Bi (blue) pairs for the lowest energy unit cell. When atom pairs of the same element are arranged in the spiral-like pattern shown in Fig. 5(a), the number of Ag–Ag/Bi–Bi interactions is minimized (only two interactions per atom), and the cell energy is also minimized. All 12 of the lowest energy structures contain the spiral pattern of Ag–Ag and Bi–Bi pairs as illustrated in Fig. 5(a). Furthermore, each unit cell is equivalent to the other through translational and rotational

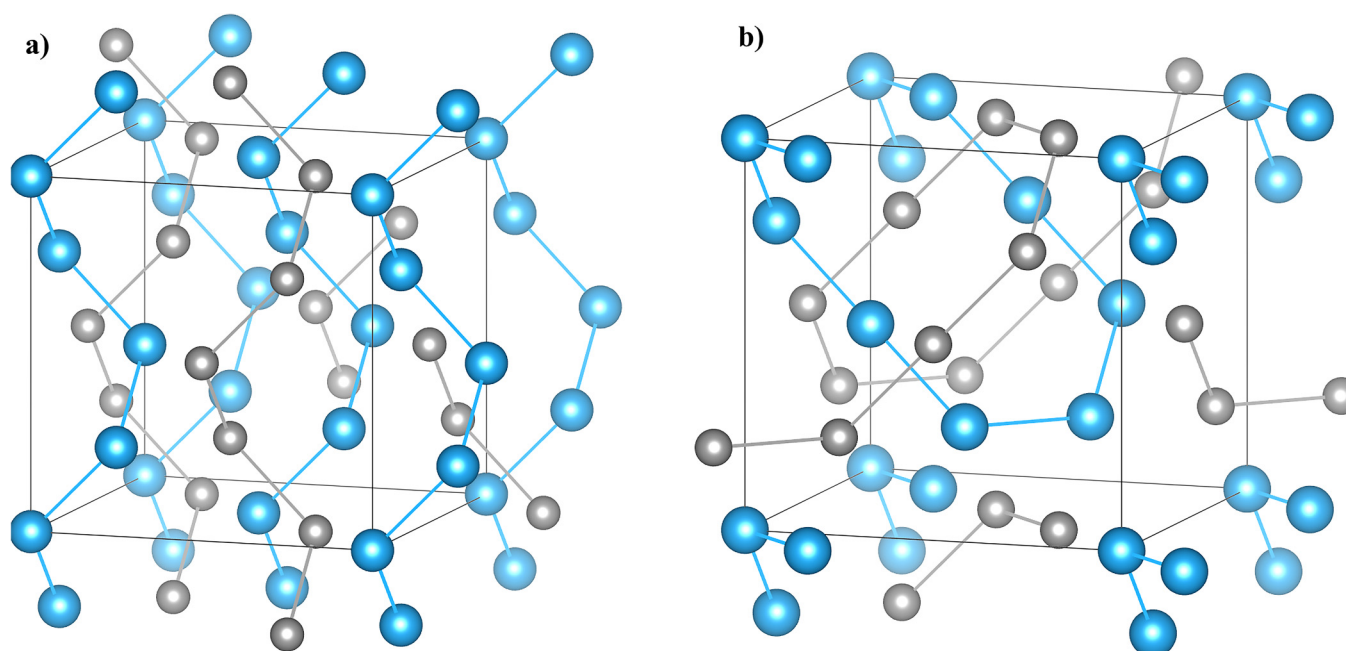


FIG. 5. Identical-element metal neighbors present in low-energy (0.0–0.25 eV bin of Fig. 2) AgBi₄ unit cells. Ag–Ag pairs (gray) and Bi–Bi pairs (blue) are shown, while both Ag–Bi pairs and I atoms are omitted for clarity. (a) Spiral-like patterns present in the lowest-energy AgBi₄ structures. Each Ag and Bi atom has two identical-element metal neighbors. (b) Second lowest-energy structures contain identical-element neighbors that loop around one another. Each atom also has two identical-element metal neighbors.

symmetries. Half have the space group $P4_322$ and the other half the space group $P4_122$.¹⁴ Note that the difference between a 4_1 and 4_3 screw axis is simply the handedness of the operation. The remaining 48 cells with slightly higher energies also contain structures that minimize the number of Ag–Ag/Bi–Bi interactions (2 per atom) but have more complicated chains of identical-element pairs. Figure 5(b), for example, shows a higher energy structure that contains identical element pairs that “loop” around one another. Each of these structures is reported to have the $C222_1$ space group. The reason for the difference in energy may be that there are fewer Ag–Bi pairs in these structures than there are in the spiral-like structures. For clarity, the Ag–Bi pairs are not connected in Fig. 5.

B. Random forest convergence

Figure 6 compares the predictions of three different versions of the RF model, as discussed above in Sec. II D. In Fig. 6(a), the RF model features include no cation pair info; in Fig. 6(b), the RF model features include cation pair info; and in Fig. 6(c), the RF model features include cation pair info and a search space reduction is applied. The blue line represents an ideal 1:1 relationship between the RF and DFT energies. In order to keep the number of training points constant between methods, the search space is reduced by a factor of 0.672 for Fig. 6(c). In all cases, 500 points were used for training. Figs. 6(a) and 6(b)’s points were selected randomly, and Fig. 6(c)’s points were selected according to the routine described at the end of Sec. II D. We test the RF model as a

function of the search space reduction factor and the number of training points. A search space reduction factor of around 0.8 (with ~350 training points) still resulted in an RF model that correctly identified the minimum energy cells consistently. Larger reductions would sometimes result in incorrect cells being identified as the minimum, and smaller reductions as used in Fig. 6(c) gave no noticeable increase in accuracy.

All three RF model predictions show a positive correlation with calculated DFT energies. Comparing Figs. 6(a) and 6(b) indicates that large improvement in RF model energies is achieved by including the cation pair data. However, in Fig. 6(b), there is still significant error in minimum energy cells; specifically, there is an energy span of about 0.4 eV near the minimum where the RF model’s standard error is around 0.12 eV. As seen in Fig. 6(c), the RF model that trains on lower energy cells results in a much more accurate prediction of lowest energy cells although the average error in energies across the entire dataset is worse. Within the same 0.4 eV energy span near the minimum energy, the accuracy of the RF model in Fig. 6(c) is about 0.02 eV—six times smaller than the error found in Fig. 6(b) results.

IV. PHYSICAL PROPERTIES

Here, we report DFT calculations for the structural and electronic properties of AgBi₄. Unless otherwise noted, all reported values are given as averages over the values in the 60 lowest energy unit cells.

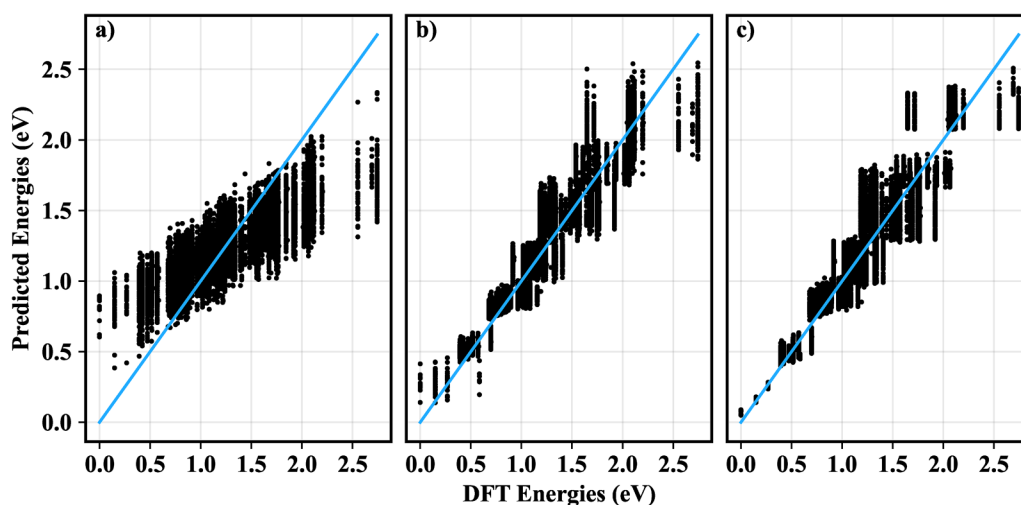


FIG. 6. Predicted energies for three different machine learning methods as a function of level 1 DFT energies from the high through-put method. (a) Only atomic positions as descriptors. (b) Atomic positions and nearest neighbor pair count as descriptors. (c) The same descriptors as in (b) but with active search-space reduction applied to bias minimum energy cells. There are many overlapping data points near the origin in (c). The blue lines represent an ideal 1:1 relationship between predicted and actual DFT energies.

A. Structural properties

We computed the average volume and extracted the average lattice constant for AgBiI_4 to be 12.71 \AA , about +4% greater than experiments^{12,29–31} but close to the previous theoretical calculations using one AgBiI_4 cell.^{10,13} The +4% deviation from experimental values is within expectations for DFT-GGA calculations. Furthermore, both Bi–I and Ag–I bond lengths were found to be 3.14 \AA , close to the experimental value of 3.09 \AA .³¹ The calculated

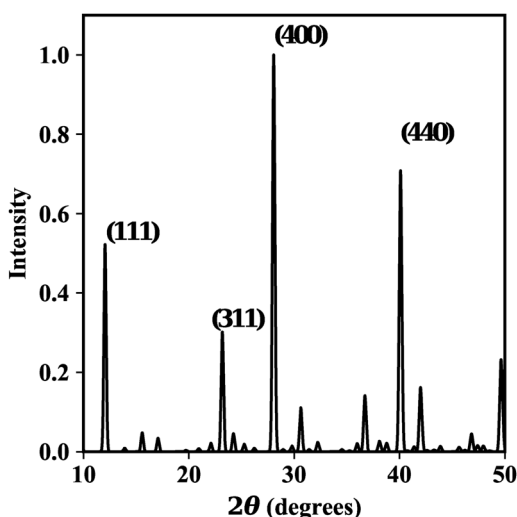


FIG. 7. Average computed x-ray diffraction pattern and Miller indices for AgBiI_4 .

density is $\rho = 5.3 \text{ g/cm}^3$ that differs from the experimental value of 6 g/cm^3 (Ref. 26) due to the aforementioned overestimation of lattice constants. This result is close to Xiao *et al.*'s theoretical value of $\rho = 5.2 \text{ g/cm}^3$.¹⁰

The simulated x-ray diffraction (XRD) pattern is reported in Fig. 7 and compares well with the experiment. In our calculations, $\lambda = 1.5406 \text{ \AA}$ (Cu K- α radiation) was used to match experimental values. Also, we used a constant Debye–Waller factor of 0.2 \AA^2 . Sansom *et al.*'s¹² experimental XRD pattern comes from polycrystalline AgBiI_4 films and has peak angle and intensities in very good agreement with our simulated XRD pattern. There is also good agreement with Ghosh *et al.*'s³² experimental XRD pattern except for their lower intensity at the (440) thin peak, possibly due to the texturing effect inherent in polycrystalline films.

B. Mechanical properties

The bulk modulus K has an average value of 7.5 GPa . This value is in between the theoretical K values for AgI ($K = 20 \text{ GPa}$) and BiI_3 ($K = 4 \text{ GPa}$).³³ For 12 lowest energy structures, $\langle K \rangle = 7.7 \text{ GPa}$, with a range of $7.3 < K < 8.3 \text{ GPa}$. The 48 higher energy structures have $\langle K \rangle = 7.5 \text{ GPa}$ and exhibit a range of values: $7.1 < K < 8.0 \text{ GPa}$. In both groups, the values of K show a single peaked, normal distribution.

C. Electronic structure

Figure 8 shows the average DOS for 60 low-energy AgBiI_4 structures split by each element's contribution. The valence band edge is set to zero. Ag's d orbital and I's p orbital are the major contributors to the DOS near the valence band maximum, while Bi's and I's p orbitals dominate near the conduction band minimum. These results are consistent with the findings from

previous theoretical studies.¹² The DOS of 12 lowest energy cells (those with the spiral-like identical-element pair topologies) and 48 higher energy cells (those with the loop-like identical-element pair topologies) are very similar except that the higher energy cells have conduction states below 2 eV. In the lowest energy cells, there are no states until after 2 eV.

The DOS in Fig. 8 is calculated with the PBE functional, but previous calculations show that including hybrid exchange and spin-orbit effects raises the bandgap slightly.¹⁰ Upon the inclusion of both hybrid exchange and spin-orbit effects for five cells, we find that the bandgap increases on average by 0.12 eV. Therefore, our theoretical estimate for the bandgap of AgBiI₄ is 1.8 eV. This is within the range of previous experimental bandgap results: 1.7,^{12,29,32} 1.8,⁶ and 1.9 eV.³⁴ The bandgap value found here also agrees with previous theoretical calculations on a single unit cell,¹⁰ since their calculations used the same exchange-correlation methods, the single unit cell they used is apparently not among the lowest energy cells we found (since we found the lowest energy cells have bandgaps greater than 2 eV).

Bandgap calculations employing the density functional theory are known to depend sensitively on the exchange-correlation functional chosen. To assess the accuracy of the PBE/HSE functionals used here, we have applied these methods to BiI₃. The physical and electronic structures of BiI₃ are well known and similar to those of AgBiI₄. Experimentally, BiI₃ has an indirect bandgap of 1.67 ± 0.09 eV.³⁵ Correcting our PBE band structure calculation with HSE calculations (as we did above for AgBiI₄), we arrive at a

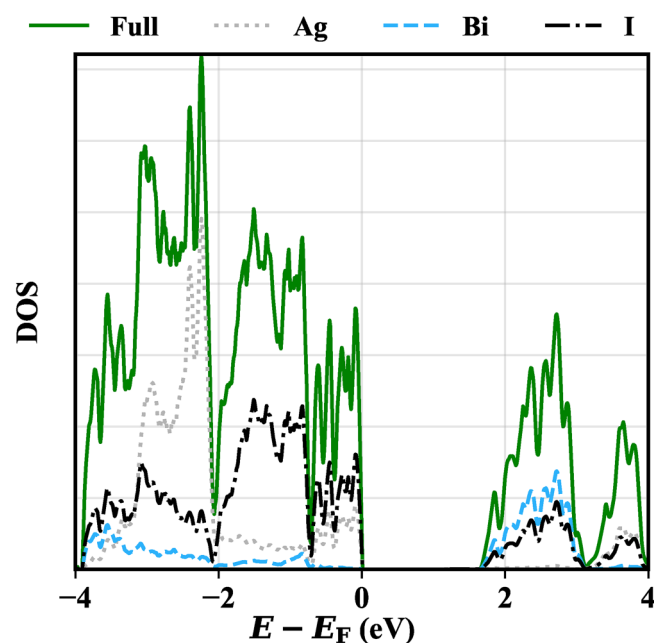


FIG. 8. Average atom-DOS for 60 lowest energy AgBiI₄ cells. Each element is plotted as the sum of its atomic orbitals, and the energy E is scaled by Fermi energy E_F . The tail of states between 1.7 and 2.0 eV are exclusively due to higher energy cells.

bandgap of 1.93 eV, which is a couple tenths of an eV higher than the highest gap value from the experimental range.

D. Effective masses

To properly account for degenerate bands and relatively flat valence bands near the band edge, we calculate a thermal average conductivity mass that includes contributions from multiple bands and their non-parabolicities. Because the higher energy group of cells have conduction band states about 0.3 eV below the lowest energy cells', electron transport is expected to be dominated exclusively by the second lowest energy group of cells. Thus, electron effective masses are only calculated with a cell from the higher energy group. On the other hand, we calculate the hole masses with a weighted average of one low energy cell's (20% contribution) and one high energy cell's (80% contribution) conductivity masses. This weighted average approximates the full averaging done in the rest of this work but is necessary because computational cost prevents the calculation of the thermal average effective mass for all 60 cells.

Figure 9 shows the average conductivity mass [calculated from the Drude model as the harmonic mean of the three eigen-masses (m^*) in AgBiI₄] plotted vs temperature for various chemical potentials. The relative masses increase monotonically with temperature from 200 to 600 K. Near room temperature, we find m^* for n-doped AgBiI₄ to be about that of a resting electron. Due to the relatively flat valence bands in AgBiI₄, hole effective masses are heavy—about seven times heavier than a resting electron at room temperature. Between 200 and 600 K, electron masses increase by about a factor of 1.6 and hole masses by about 1.8.

In general, m^* increases with temperature, since raising the temperature thermally activates (1) non-parabolic portions of bands and (2) states further from the band edges, which tend to be flatter than states at band edges. These two effects also explain why m^* increases as the Fermi energy moves closer to band edges.

E. Band structure

A better understanding of the thermal average conductivity mass can be obtained through an inspection of band energies. Figure 10(a) shows the energy-map of the lowest energy cell's valence band while Fig. 10(b) shows the energy-map for conduction band edges of a cell from the second lowest energy group. In Fig. 10, the important Γ point is in the center of the solid cube. To view the band energies around Γ , 1/8th of the Brillouin zone is removed. Be aware of the different energy scaling between Figs. 10(a) and 10(b).

In Fig. 10(a), the red-orange domains of high energy and low curvature extend from Γ most dramatically to the zone edges in the $\pm k_x$ direction. These shallow energy regions result in high effective hole masses even below room temperature. Figure 10(c) shows secondary bands that will affect hole masses at elevated temperatures. From Fig. 10(d), one can see that at the R point, two bands are nearly degenerate, with the higher energy band having a higher energy curvature. The energy difference between these two bands is small enough that the thermal average takes the higher curvature band into account except at temperatures far below room temperature.

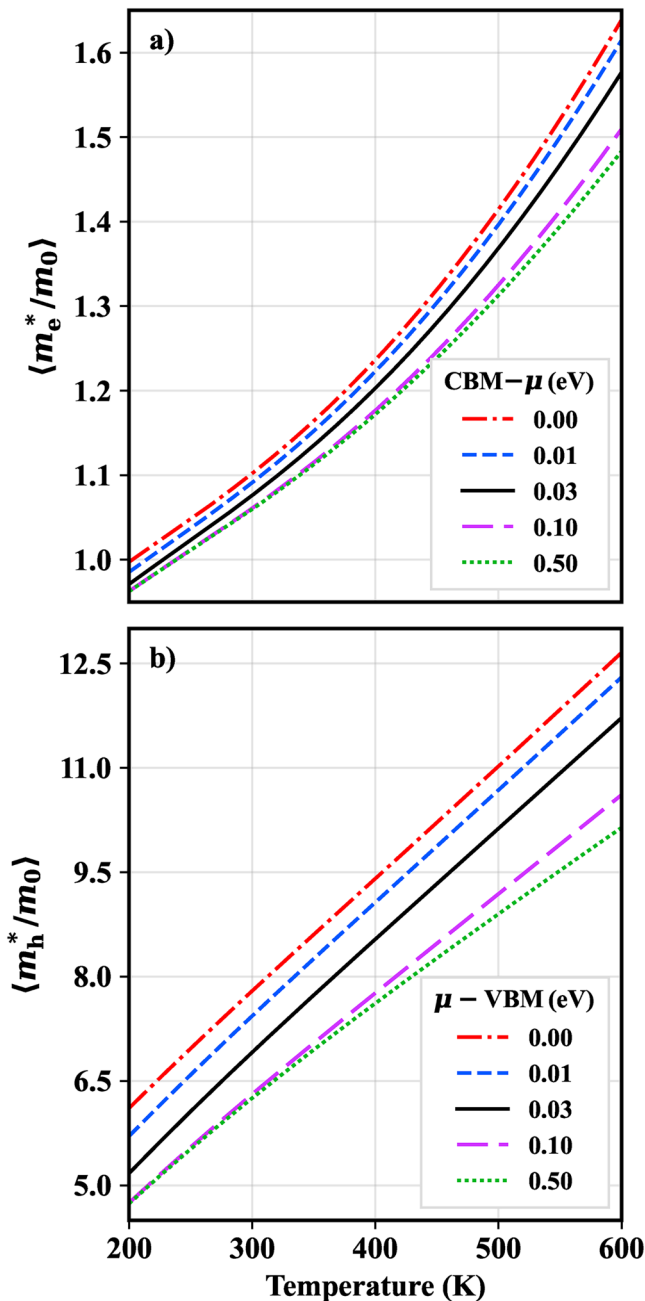


FIG. 9. Conductivity (a) electron and (b) hole effective masses in AgBiI₄. Averages are taken over the three characteristic directions calculated from the full m^* tensor. Chemical potential values, μ , are given relative to their relevant band maxima.

Even at temperatures below room temperature, the conductivity masses can significantly differ from effective masses calculated with the standard parabolic approximation. For example, consider the valence bands in a low energy cell of AgBiI₄ [Figs. 10(a)

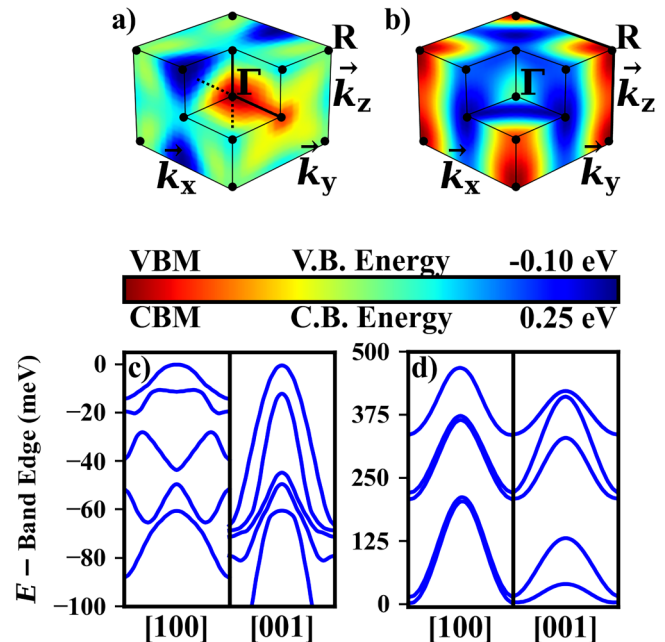


FIG. 10. Energies of the valence band edge (a) and conduction band edge (b) in the first Brillouin zone of AgBiI₄. In (a), black lines originating from the VBM (Γ) represent paths that the valence band diagrams (c) are calculated along. Similarly, in (b), black lines originating from CBM (R) represent paths that the conduction band diagrams (d) are calculated along.

and 10(c)]. In the [100] direction [corresponding to the direction of spiral patterns in Fig. 5(a)], bands at the band edge are very shallow—the difference between the top and bottom of the band maxima band is only about 15 meV. This means that even at 87 K ($k_B T = 7.5$ meV), about half of the entire band is thermally activated. Additionally, the second topmost band is about 10 meV below the VBM, meaning that it will begin contributing to the average mass at around 120 K. As for conduction bands, the near-degenerate (10 meV difference in energies at the R point) bands at the conduction band edge [Fig. 10(d)] exhibit similar curvatures in two of three directions, but the curvature of the higher energy band in the [001] direction significantly lowers the thermal average mass compared to only considering the lowest energy band in parabolic approximation. This effect should also be seen at about 120 K.

Pecunia *et al.*¹³ recently used the parabolic approximation to calculate effective masses in AgBiI₄. For electrons, they report conductivity masses of $1.1 m_0$ that coincides with the present conductivity result at 200 K. This good agreement is due to the harmonic averaging method—the lightest, middle, and heaviest electron masses from Pecunia *et al.* are $0.9 m_0$, $1.1 m_0$, and $1.3 m_0$, while our thermal average results at 200 K are $0.7 m_0$, $0.7 m_0$, and $3.8 m_0$. Although the individual masses differ, the average yields similar results. The previously reported conductivity mass of $4.3 m_0$ is lower than our hole mass of $5.2 m_0$ at 200 K. Deviations between previous results and present results are likely due to both choice of unit cell(s) as well as previously discussed differences between

thermal averaging and parabolic approximations to calculate the effective mass. As one would expect from the complicated valence bands of AgBiI_4 , the differences between the parabolic results and thermal average results are larger for holes than for electrons and become increasingly larger at elevated temperatures.

V. CONCLUSION

By calculating the energies of all possible AgBiI_4 unit cells, we have determined a subset of cells that, when considered as an ensemble, produces results consistent with experiments. With these cells, we predict the material's mechanical and electrical properties, including the conductivity effective masses. For the latter, we quantify the variation in average band masses as a function of temperature and Fermi energy.

Additionally, we showcase a simple random forest model that is capable of accurately determining the lowest energy cells with a computational load reduced by a factor of 25. For predicting the final relaxed DFT energies of AgBiI_4 , bonding topology was found to be an important factor. Combining a simple set of machine learning descriptors with an aggressive reduction of the unit cell search space allowed for the accurate classification of lowest-energy unit cells. We believe that this method should be useful for solving similar problems involving large numbers of unit cells.

For properties such as the lattice constant and powder XRD pattern, many unit cells reproduce experimental results well. We predict that AgBiI_4 has a bulk modulus more similar to BiI_3 than to bulk AgI. The DOS shows that Ag and I states make up the majority of the upper valence band, while the lower conduction band is comprised of Bi and I states, consistent with Ref. 12. For AgBiI_4 's use in devices, average conductivity mass calculations indicate that relying on holes for charge transport will be very inefficient on account of their heavy masses, while electrons should provide more reasonable transport properties. These results are consistent with the band structure of AgBiI_4 , which exhibits a high density of flat valence bands near the VBM, and a few conduction bands with higher curvatures near the CBM.

Of course, the properties of the whole material are not guaranteed to be the average of individual unit cell results. Nevertheless, the unit cells identified herein present a proper starting point for the study of the role of larger scale structures and for examining the properties of defects in AgBiI_4 . Furthermore, our approach and findings provide a platform for future studies of structural and electronic properties of other silver iodo-bismuthate compounds and related metal-halide semiconductors.

ACKNOWLEDGMENTS

B.R.T. would like to acknowledge support from the National Science Foundation (NSF) under Grant No. DMR-2127473. Computations for this research were performed on the Pennsylvania State University's Institute for Computational and Data Sciences' Roar supercomputer and the Ohio Supercomputer Center's Owens supercomputing cluster.³⁶ This material is also based on research sponsored by the Air Force Research Laboratory under Agreement No. FA9453-19-C-1002 and the National Science Foundation Division of Civil, Mechanical, and Manufacturing Innovation under Grant No. 1629239. The U.S. Government is

authorized to reproduce and distribute reprints for Governmental purposes not withstanding any copyright notation thereon. The views and conclusions contained herein are those of the authors and should not be interpreted as necessarily representing the official policies or endorsements, either expressed or implied, of Air Force Research Laboratory or the U.S. Government.

AUTHOR DECLARATIONS

Conflict of Interest

The authors have no conflicts to disclose.

DATA AVAILABILITY

The data that support the findings of this study are available from the corresponding author upon reasonable request and are openly available in GitHub page (VictorBarone5066), <https://github.com/VictorBarone5066/PublicationData-PropertiesAgBiI4-ML>.

REFERENCES

- 1A. K. Jena, A. Kulkarni, and T. Miyasaka, "Halide perovskite photovoltaics: Background, status, and future prospects," *Chem. Rev.* **119**(5), 3036–3103 (2019).
- 2D. H. Fabini *et al.*, "Main-group halide semiconductors derived from perovskite: Distinguishing chemical, structural, and electronic aspects," *Inorg. Chem.* **56**(1), 11–25 (2017).
- 3J.-C. Hebig, I. Kühn, J. Flohre, and T. Kirchartz, "Optoelectronic properties of $(\text{CH}_3\text{NH}_3)_3\text{Sb}_2\text{I}_9$ thin films for photovoltaic applications," *ACS Energy Lett.* **1**(1), 309–314 (2016).
- 4S. Sun, S. Tominaka, J.-H. Lee, F. Xie, P. D. Bristowe, and A. K. Cheetham, "Synthesis, crystal structure, and properties of a perovskite-related bismuth phase, $(\text{NH}_4)_3\text{Bi}_2\text{I}_9$," *APL Mater.* **4**(3), 031101 (2016).
- 5G. Kakavelakis, M. Gedda, A. Panagiotopoulos, E. Kymakis, T. D. Anthopoulos, and K. Petridis, "Metal halide perovskites for high-energy radiation detection," *Adv. Sci.* **7**(22), 2002098 (2020).
- 6I. Turkevych *et al.*, "Photovoltaic rudorffites: Lead-free silver bismuth halides alternative to hybrid lead halide perovskites," *ChemSusChem* **10**(19), 3754–3759 (2017).
- 7H. Zhu, M. Pan, M. B. Johansson, and E. M. J. Johansson, "High photon-to-current conversion in solar cells based on light-absorbing silver bismuth iodide," *ChemSusChem* **10**(12), 2592–2596 (2017).
- 8A. Crovetto, A. Hajjifarassat, O. Hansen, B. Seger, I. Chorkendorff, and P. C. K. Vesborg, "Parallel evaluation of the BiI_3 , BiOI , and Ag_3BiI_6 layered photoabsorbers," *Chem. Mater.* **32**(8), 3385–3395 (2020).
- 9V. Pecunia, "Efficiency and spectral performance of narrowband organic and perovskite photodetectors: A cross-sectional review," *J. Phys. Mater.* **2**, 042001 (2019).
- 10Z. Xiao, W. Meng, D. B. Mitzi, and Y. Yan, "Crystal structure of AgBi_2I_7 thin films," *J. Phys. Chem. Lett.* **7**(19), 3903–3907 (2016).
- 11L. F. Mashadiyeva, Z. S. Aliev, A. V. Shevelkov, and M. B. Babanly, "Experimental investigation of the Ag–Bi–I ternary system and thermodynamic properties of the ternary phases," *J. Alloys Compd.* **551**, 512–520 (2013).
- 12H. C. Sansom *et al.*, "Agbii₄ as a lead-free solar absorber with potential application in photovoltaics," *Chem. Mater.* **29**(4), 1538–1549 (2017).
- 13V. Pecunia *et al.*, "Assessing the impact of defects on lead-free perovskite-inspired photovoltaics via photoinduced current transient spectroscopy," *Adv. Energy Mater.* **11**(22), 2003968 (2021).
- 14A. Togo and I. Tanaka, "A software library for crystal symmetry search," arXiv: [cond-mat.mtrl-sci] 2018 (2018).
- 15G. Kresse and J. Furthmüller, "Efficient iterative schemes for *ab initio* total-energy calculations using a plane-wave basis set," *Phys. Rev. B* **54**, 11169 (1996).

- ¹⁶G. Kresse and J. Hafner, “*Ab initio* molecular dynamics for liquid metals,” *Phys. Rev. B* **47**, 558 (1993).
- ¹⁷G. Kresse and J. Furthmüller, “Efficiency of *ab-initio* total energy calculations for metals and semiconductors using a plane-wave basis set,” *Comput. Mater. Sci.* **6**, 15–50 (1996).
- ¹⁸P. Hohenberg and W. Kohn, “Inhomogeneous electron gas,” *Phys. Rev.* **136**, B864 (1964).
- ¹⁹W. Kohn and L. J. Sham, “Self-consistent equations including exchange and correlation effects,” *Phys. Rev.* **140**, A1133 (1965).
- ²⁰J. P. Perdew, K. Burke, and M. Ernzerhof, “Generalized gradient approximation made simple,” *Phys. Rev. Lett.* **77**, 3865 (1996).
- ²¹P. E. Blöchl, “Projector augmented-wave method,” *Phys. Rev. B* **50**, 17953 (1994).
- ²²G. Kresse and D. Joubert, “From ultrasoft pseudopotentials to the projector augmented-wave method,” *Phys. Rev. B* **59**, 1758 (1999).
- ²³V. T. Barone, “VBHTC,” available at: <https://github.com/victorbarone5066>.
- ²⁴S. Curtarolo, G. L. W. Hart, M. B. Nardelli, N. Mingo, S. Sanvito, and O. Levy, “The high-throughput highway to computational materials design,” *Nat. Mater.* **12**, 191–201 (2013).
- ²⁵R. Armiento, B. Kozinsky, M. Fornari, and G. Ceder, “Screening for high-performance piezoelectrics using high-throughput density functional theory,” *Phys. Rev. B* **84**, 014103 (2011).
- ²⁶J. Heyd, G. E. Scuseria, and M. Ernzerhof, “Hybrid functionals based on a screened Coulomb potential,” *J. Chem. Phys.* **118**, 8207–8215 (2003).
- ²⁷G. Hautier, A. Miglio, D. Waroquiers, G.-M. Rignanese, and X. Gonze, “How does chemistry influence electron effective mass in oxides? A high-throughput computational analysis,” *Chem. Mater.* **26**, 5447–5458 (2014).
- ²⁸F. Pedregosa *et al.*, “Scikit-learn: Machine learning in Python,” *J. Mach. Learn. Res.* **12**, 2825–2830 (2011).
- ²⁹M. Khazaei *et al.*, “Dual-source evaporation of silver bismuth iodide films for planar junction solar cells,” *J. Mater. Chem. A* **7**, 2095–2105 (2019).
- ³⁰C. Lu *et al.*, “Inorganic and lead-free AgBiI₄ ruderfite for stable solar cell applications,” *ACS Appl. Energy Mater.* **1**, 4485–4492 (2018).
- ³¹T. Oldag, T. Aussieker, H.-L. Keller, C. Preitschaft, and A. Pfitzner, “Solvothermale Synthese und Bestimmung der Kristallstrukturen von AgBiI₄ und Ag₃BiI₆,” *Z. Anorg. Allg. Chem.* **631**, 677–682 (2005).
- ³²B. Ghosh *et al.*, “Superior performance of silver bismuth iodide photovoltaics fabricated via dynamic hot-casting method under ambient conditions,” *Adv. Energy Mater.* **8**, 1802051 (2018).
- ³³M. de Jong *et al.*, “Charting the complete elastic properties of inorganic crystalline compounds,” *Scientific Data* **2**, 150009 (2015).
- ³⁴S. Lu, Q. Zhou, Y. Ouyang, Y. Guo, Q. Li, and J. Wang, “Accelerated discovery of stable lead-free hybrid organic-inorganic perovskites via machine learning,” *Nat. Commun.* **9**, 3405 (2018).
- ³⁵N. J. Podraza *et al.*, “Band gap and structure of single crystal BiI₃: Resolving discrepancies in literature,” *J. Appl. Phys.* **114**, 033110 (2013).
- ³⁶Ohio Supercomputer Center’s Owens Supercomputing Cluster; available at: <https://www.osc.edu/>.